Article | Open Access

Energy Materials

Zou et al. Energy Mater. 2026, 6, 600074 DOI:10.20517/energymater.2026.87

Heteroatom-driven the rapid electrochemical process of anthracite derivatives in sodium-ion battery

Lianli Zou*, Tongbo Yang, Longwei Li, Ling Lin, Maoxiang Jing, Qiuju Wang*

Keywords:
Anthracite, carbon anode, sodium-ion battery, heteroatoms; doping

Citation: Zou, L.; Yang, T.; Li, L.; Lin, L.; Jing, M.; Wang, Q. Heteroatom-driven the rapid electrochemical process of anthracite derivatives in sodium-ion battery. *Energy Mater.* **2026**, *6*, 600074. https://dx.doi.org/10.20517/energymater.2026.87

Received: 25 Apr 2026
First Decision: 29 May 2026
Revised: 6 Jun 2026
Accepted: 16 Jun 2026
Published: 3 Jul 2026

Academic Editor: Yuping Wu
Copy Editor: Shu-Yuan Duan
Production Editor: Shu-Yuan Duan

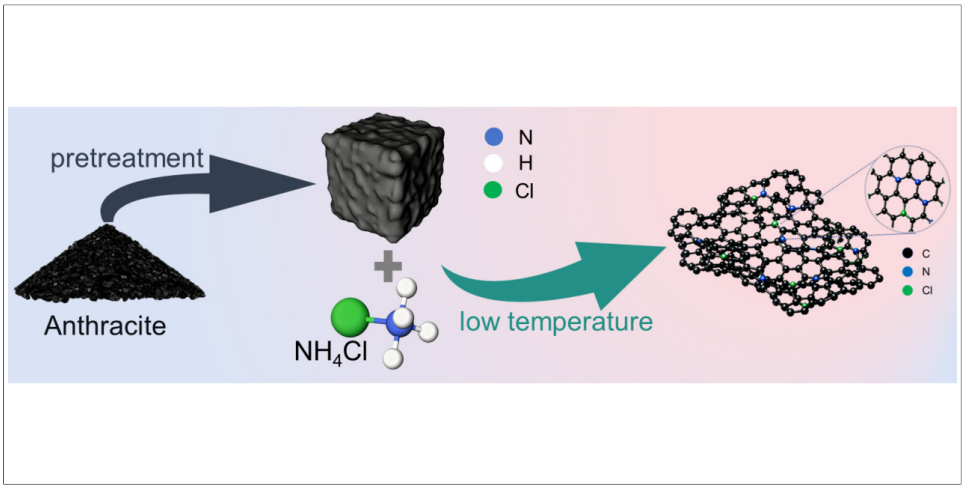

Abstract

Anthracite exhibits great potential for anodes in sodium-ion batteries (SIBs) attributed to its rich reserve and high carbon content. Here, a high-performance anthracite-derived carbon with both N and Cl doping (ACp-N-Cl) was prepared by a low-temperature pyrolysis process, which showed a large reversible capacity and enhanced rate capability for SIBs. Calcining the purified anthracite and ammonium chloride in an inert atmosphere at 400 °C resulted in a porous carbon engineered with numerous edge defects and topological irregularities, which were beneficial to the storage of Na^+ by lowering the ion migration energy barrier. The obtained ACp-N-Cl electrode materials exhibited outstanding electrochemical performances in both rate capability and long-term stability, delivering a discharge capacity of 220 mAh g^{-1} (@0.02 A g^{-1}) after 50 cycles and retaining a capacity of 173 mAh g^{-1} after 8000 cycles at 1 A g^{-1}. Kinetic analysis confirmed that the performance enhancement was primarily attributed to the increased pseudocapacitive contribution and improved ion transport by N and Cl heteroatoms doping. This study offers a promising method to produce carbon anodes from low-cost coal-based precursors, which is practicable for a large-scale production.

Institute for Advanced Materials, School of Materials Science and Engineering, Jiangsu University, Zhenjiang 212013, Jiangsu, China.

*Correspondence to: Dr. Lianli Zou, Dr. Qiuju Wang, Institute for Advanced Materials, School of Materials Science and Engineering, Jiangsu University, Zhenjiang 212013, Jiangsu, China. E-mail: lianli_zou@ujs.edu.cn; wang_qiuju@ujs.edu.cn

INTRODUCTION

With increasing global energy constraints and the rapid expansion of renewable energy demand, efficient and cost-effective energy storage technologies have become critical to the modernization of energy systems. Although lithium-ion batteries are already widely commercialized, sodium-ion batteries (SIBs) have aroused great attention in recent years because of the abundant reserves and low-cost features of sodium compared with lithium resources[1-4]. For SIBs, the chemistry and architecture of anode material strongly affect Na^+ storage kinetics, capacity retention, and overall rate behavior. Carbonaceous materials are regarded as highly promising candidates, as their tailored pore structures provide favorable sites and pathways for accommodating the relatively large Na^+ ions.

Among various carbon materials, anthracite is an ideal precursor due to its high carbon content, low ash content, and low cost[5-8]. However, anthracite also has several drawbacks when directly used as an anode for SIBs. Its native structure is relatively dense, with a small interlayer spacing and a limited number of active sites, which results in low reversible capacity, slow Na^+ insertion/extraction kinetics, and poor rate performance, hindering the practical application of anthracite-based anode materials. Most modification strategies for preparing hard carbon from anthracite mainly relied on high-temperature modification, which tailors the microstructure by expanding the interlayer spacing and constructing closed pore structures[9,10]. As one of the most widely used methods, high-temperature treatment not only consumes large amounts of energy, but also involves complicated procedures and low yields of products, leading to the increase of production costs. Therefore, low-temperature treatment to fabricate anthracite-derived carbon has garnered considerable interest. Despite its advantages in yields and production costs, low-temperature treatment still suffers from issues including low electronic conductivity and poor structural stability, and the relatively low capacity and poor rate performance limit its practical applications[11,12].

To increase the accessible active sites for Na^+ storage, pore construction and defect engineering are effective strategies, and etching agents or dopants are commonly introduced during synthesis. As a thermally volatile pore-forming additive, ammonium chloride (NH_4Cl) is commonly employed to construct pores, boost carbon wettability and speed up ionic diffusion in carbon substrates[13,14]. Owing to the existence of N and Cl in NH_4Cl, it can be used alone as either a nitrogen source or a chlorine source for carbon doping. However, achieving N and Cl co-doping by using NH_4Cl as a dual dopant and simultaneously as an etching agent is difficult, and few reports have described this strategy, to the best of our knowledge. This is attributed to the fact that the use of NH_4Cl as dopants is highly dependent on the heat-treatment temperature. When the temperature is high, NH_4Cl decomposes into gaseous species that etch the carbon material, rather than reacting with the carbon matrix[15]. In this work, anthracite was doped with N and Cl heteroatoms through a low-temperature treatment using NH_4Cl as both a dopant and an etching agent. This process not only introduced N and Cl but also modified the pore structure of anthracite via etching, resulting in a high-quality anode material for SIBs. Attributed to the doped N and Cl, especially with nitrogen doping, which improved the accessible active sites and drove the ion transport, along with the etching role of NH_4Cl that enlarged average pore size of anthracite for fast Na^+ transport, the anthracite-derived materials achieved favorable rate behavior and long-cycle durability, maintaining a discharge capacity of 173 mAh g^{-1} with nearly no decay at 1 A g^{-1} even after 8,000 cycles.

EXPERIMENTAL SECTION

Materials synthesis

Anthracite from the Hebei region of China was used as a carbon precursor. Initially, 5 g of anthracite was subjected to high-energy ball milling with ethanol at 800 rpm for 8 h. The resulting sample was dried, sieved, and recorded as C. Then, HCl and HF were used to remove impurity components through a hydrothermal process, and the obtained product was denoted as Cp. The pre-oxidized anthracite, designated as ACp, was

prepared by heating Cp in air at 400 °C for 4 h with a rate of 5 °C· min^{-1}. Finally, ACp and NH_4Cl were mixed at mass ratios of 2:1, and the resulting solids were heated in a nitrogen atmosphere by ramping the temperature from room temperature to 400 °C at 5 °C min^{-1} and held for 4 h. This sample was denoted as ACp-N-Cl. When ACp was mixed with other kinds of salts, the samples were denoted as ACp-X (X= NaCl, KCl or NH_4Br).

Materials characterization

The crystalline structures of samples were examined by X-ray diffraction (XRD, Smart Lab), and their morphologies were recorded by scanning electron microscopy (SEM, JSM-7800F). Transmission electron microscopy (TEM) observations and elemental mapping images were carried out on a JEOL JEM-2100F microscope at 200 kV. N_2 adsorption–desorption tests were performed at 77 K with a TriStar II 3020 analyzer, and the obtained isotherms were used to determine the surface area and pore parameters. Surface elemental states were probed by X-ray photoelectron spectroscopy (XPS) on an ESCALAB QXi instrument using monochromatic Al Kα radiation. Raman measurements were conducted with a DXR laser micro-Raman spectrometer. Fourier transform infrared (FTIR) spectra were collected on an FTIR-850 instrument to identify the surface functional groups. Other instrument-related details are summarized in Supplementary Table 1.

Electrochemical measurements

Using the as-prepared samples as the active materials, CR2032 coin cells were assembled in a Mikrouna glovebox under Ar protection, where both water and oxygen levels were controlled below 0.01 ppm. For preparing electrodes, active materials and Poly(vinylidenefluoride) with a weight ratio of 85:15 were kneaded together, and N-methyl-2-pyrrolidone (NMP) was subsequently added to form a slurry. After coated on Al foils, the electrodes were dried in a vacuum oven at 120 °C for overnight, giving a mass loading of 1.0-1.5 mg cm^{-2}. In the half-cell configuration, $NaPF_6$ was used as the electrolyte, metallic Na was adopted as the counter side, and glass fiber acted as the separating membrane. Before galvanostatic charge/discharge recording, each cell was first activated twice at 0.02 A g^{-1}. Cyclic voltammetry (CV) curves were collected on a CHI 660E workstation from 0.01 to 3.0 V versus Na/Na^+. Electrochemical impedance spectroscopy (EIS) spectra were measured at a frequency of 0.01-100,000 Hz. Rate capability, long-term durability, and galvanostatic intermittent titration technique (GITT) measurements were tested at room temperature on a LAND CT 2001C battery testing system. GITT was performed with a pulse current of 0.02 A g^{-1}, with a 15 min rest period after every 30 min pulse.

RESULTS AND DISCUSSION

Structure characterization

Purified anthracite was used as the precursor to synthesize ACp-N-Cl [Figure 1A], which showed micro-sized flaky particles and no obvious change in surface morphology before and after functionalization [Figure 1B and Supplementary Figures 1-3]. There were numerous impurities in the C sample [Supplementary Figure 1 and Supplementary Table 2], while the Cp mainly consisted of only carbon, oxygen and a very limited part of nitrogen after acid washing [Supplementary Figure 2], suggesting that the acid treatment effectively removed mineral impurities[16]. As shown in Supplementary Figure 3, the oxygen content in ACp reached the highest value (about 21.94%), owing to the pre-oxidation process[17]. TEM images [Figure 1C and D] revealed that the ACp-N-Cl possessed a thin-sheet-like structure that was mainly composed of disordered carbon with lots of nanosized pores, which allow Na^+ to move along multiple directions and facilitate the infiltration of electrolyte in carbon anodes. As shown in Figure 1E, energy-dispersive spectroscopy (EDS) mapping results revealed that the sample was composed of C, N, O and Cl elements, in which the nitrogen content reached 15.96 % [Supplementary Table 2].

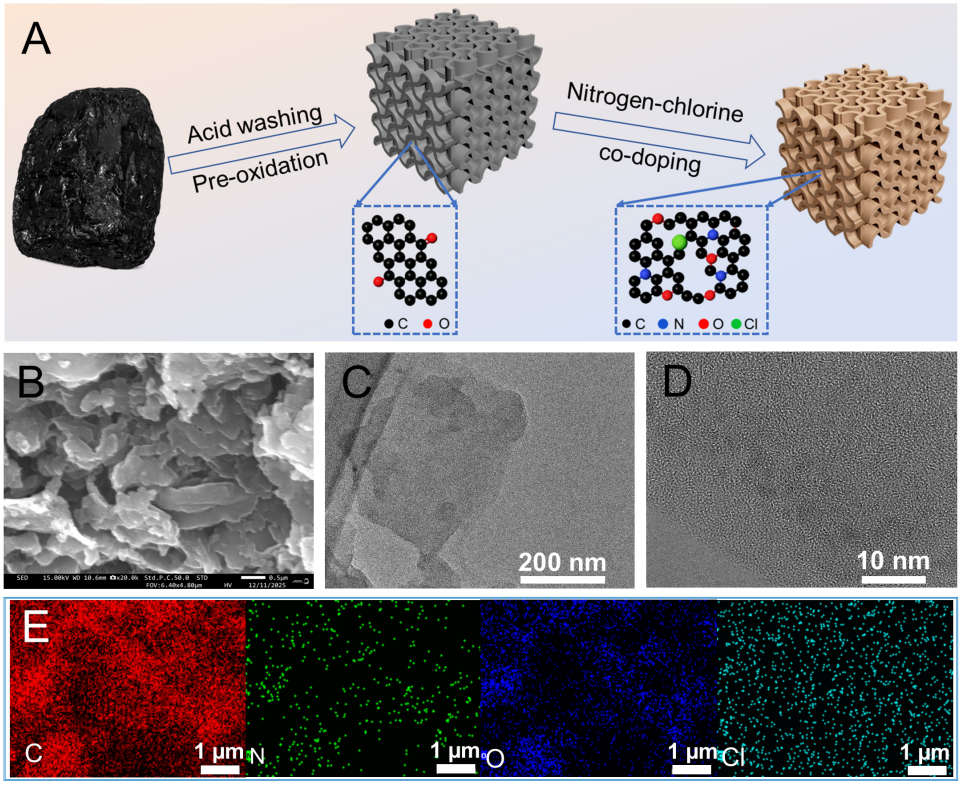

Figure 1. (A) Schematic diagram for the synthetic process, (B) SEM, (C and D) TEM and (E) EDS mapping images of ACp-N-Cl. SEM: Scanning electron microscopy; TEM: transmission electron microscopy; EDS: energy-dispersive spectroscopy.

Diffraction profiles for the obtained materials are shown in Figure 2A. Two peaks centered at about 25.0° and 43.5° [Supplementary Table 3] corresponded to crystal planes of (002) and (100), respectively, indicating the disordered structure of carbon materials[18]. The impurity-related peaks observed in C indicated the presence of mineral impurities. After acid washing, the diffraction peaks related to these impurities disappeared. To quantitatively analyze the detailed microcrystalline structure of the as-prepared materials, we further calculated the interlayer spacing (d-(hkl)), crystallite length (L_a), and crystallite stacking thickness (L_c) based on the powder X-ray diffraction results [Supplementary Figure 4 and Supplementary Table 3]. It is well known that a large spacing facilitates the Na^+ intercalation and deintercalation. Owing to the overall interlayer spacing of the materials in this work was relatively small [Supplementary Table 3], the contribution of intercalation to the total capacity was limited, and the capacity mainly originated from other mechanisms such as defect adsorption and pore filling. Among these samples, the ACp-N-Cl with a proper L_a possessed the smallest L_c value, which suggested that the co-doping of nitrogen and chlorine improved the structural disorder of the material, providing abundant accessible sites for sodium storage [Supplementary Table 3]. As shown in FTIR curves [Figure 2B], obvious C=C adsorption peaks near 1,585 cm^{-1} were observed in all samples. After pre-oxidation, the kinds of oxygen-containing groups such as C=O (1,710 cm^{-1}) and C-O (1,030-1,235 cm^{-1}) increased, indicating that pre-oxidation facilitated the introduction of oxygen-containing functional groups[19]. Compared with ACp, these signals slightly decreased in ACp-N-Cl, which was consistent with the EDS results [Supplementary Table 2]. The OH vibrations (3,345-3,450 cm^{-1}) in these samples indicated their hydrophilicity properties[20].

Raman spectra were used to identify the defect sites in the samples [Figure 2C], and the disorder degree of carbon was evaluated by using the height ratio of D band to G band (I_D/I_G)[21]. Two prominent peaks centered at approximately 1,352 (D band) and 1,581 cm^{-1} (G band) were observed for all samples. The detailed fitting

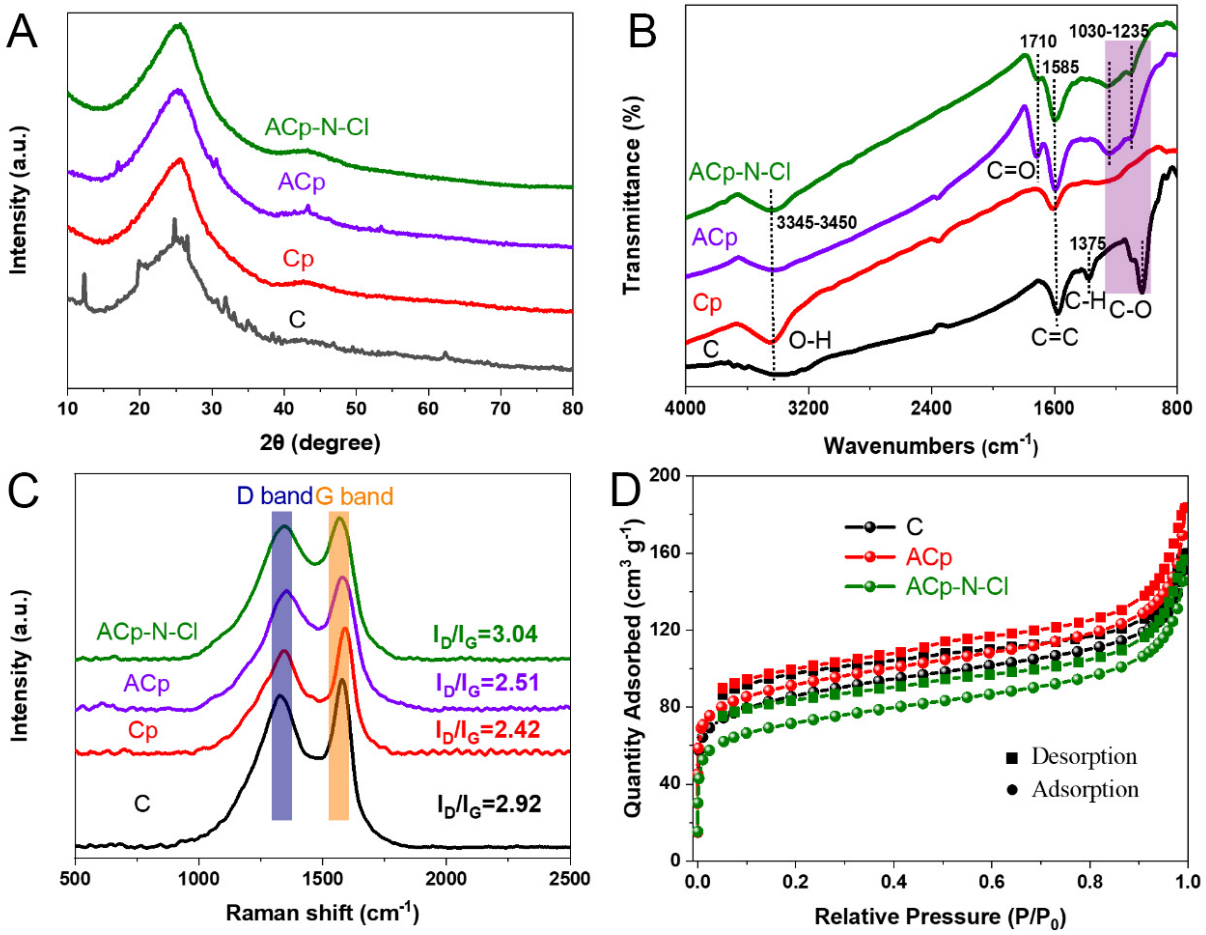

Figure 2. (A) XRD patterns, (B) FTIR spectra and (C) Raman spectra, and (D) N_2 adsorption/desorption curves of C, ACp, and ACp-N-Cl. XRD: X-ray diffraction; FTIR: Fourier transform infrared.

process of the Raman spectra and the parameters for calculating the I_D/I_G ratio are displayed in Supplementary Figure 5 and Supplementary Table 4. The I_D/I_G ratios of C, Cp, ACp and ACp-N-Cl, calculated based on the integrated areas of the fitted D and G peaks, were 2.92, 2.42, 2.51, and 3.04, respectively. The relatively large I_D/I_G ratio of C might be attributed to the presence of impurities. Through the pre-oxidation, the number of defect sites increased. It was noted that the ACp-N-Cl possessed the highest concentration of defects, confirming the entry of N/Cl species into the carbon skeleton. N_2 adsorption-desorption curves are shown in Figure 2D. The Brunauer-Emmet-Teller (BET) surface areas of C, ACp and ACp-N-Cl were 317.39, 339.57 and 265.90 $m^2 g^{-1}$, respectively, with average pore sizes mainly concentrated within 5 nm [Supplementary Figure 6]. Compared with ACp, the ACp-N-Cl displayed a decrease in BET surface area and pore volume after heating with NH_4Cl, which might be attributed to the partial collapse of the carbon structure by the substitution of O with N and Cl atoms during the calcination process. Of course, the average pore size of ACp-N-Cl was enlarged to 8.06 nm, attributed to the intrinsic etching role of NH_4Cl [Supplementary Table 5]. Additionally, this moderately enlarged pore size may facilitate ion transport and accommodate solvated Na^+ ions during the electrochemical process.

XPS results were presented in Figure 3A, and the survey spectrum of these samples showed three main binding-energy peaks, which can be indexed as C 1s, N 1s, and O 1s features. The high-resolution C 1s spectra in Figure 3B could be deconvoluted into three peaks centered at 284.7, 286.3, and 288.2 eV, corresponding to C-C, C-O, and C=O species, respectively[22]. The variation of oxygen-containing groups

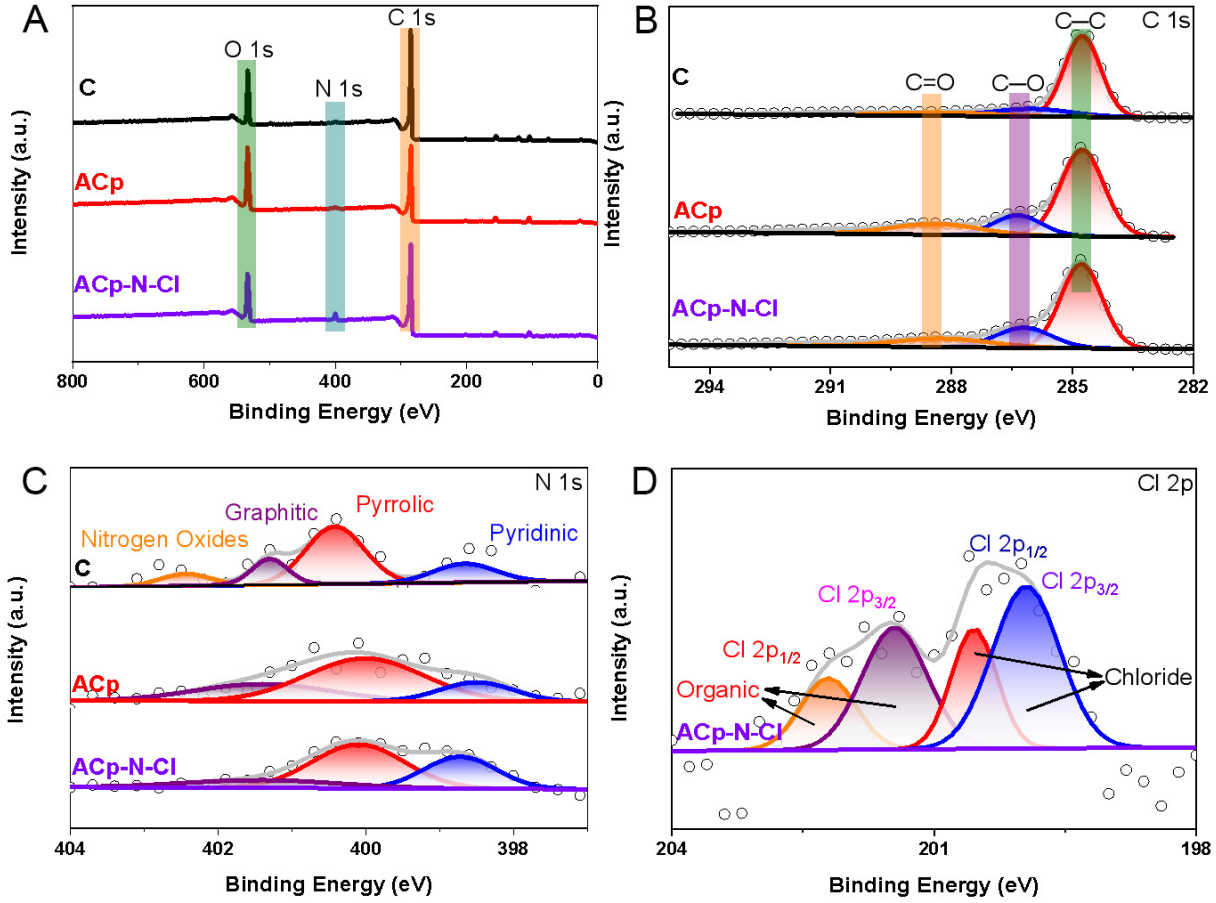

Figure 3. (A) XPS survey spectra and high-resolution spectra for (B) C 1s, (C) N 1s and (D) Cl 2p of ACp-N-Cl. XPS: X-ray photoelectron spectroscopy.

agreed with the FTIR analysis and was also evidently found in the survey spectrum[23]. N 1s spectra of ACp and ACp-N-Cl displayed three similar peaks at 398.7, 400.2 and 401.6 eV [Figure 3C], attributed to the formation of pyridinic, pyrrolic and graphite N species, respectively. The absence of the nitrogen oxide-related peak in pristine C was likely associated with residual impurities, following the indication from XRD profiles. In addition, the N 1s signal of ACp-N-Cl was more pronounced than those of other samples, suggesting an increased nitrogen content after N doping[24,25]. Moreover, a clear response was detected in the Cl 2p region [Figure 3D], suggesting that the used NH_4Cl during pyrolysis not only served as a nitrogen source but also allowed chlorine species to enter into the carbon framework. The Cl 2p spectrum [Figure 3D] included organic and inorganic chlorine, which displayed four peaks at 199.7, 200.4, 201.5 and 202.4 eV. The organic chlorine species confirmed the existence of C-Cl bonds in ACp-N-Cl, indicating that part of the Cl atoms were chemically incorporated within the carbon framework[26,27]. This kind of Cl species could induce the local charge redistribution around adjacent carbon atoms, thereby stabilizing the carbon structure and serving as additional structural defects[28]. The inorganic chlorine species originated from adsorbed free chloride ions after NH_4Cl treatment, which might also act as sodium storage sites due to their high electronegativity.

Electrochemical performance

The reversible charge-discharge curves of C, Cp, ACp and ACp-N-Cl using coin cells at 0.02 A g^{-1} were presented in Figure 4A. The initial coulombic efficiency of these four samples from C to ACp-N-Cl increased gradually [Supplementary Figure 7 and Supplementary Table 6]. The curve inflections near 3.0 V were

observed for the C and Cp not only during the initial charging process but also in the subsequent charge curves upon cycling]Figure 4a and Supplementary Figure 8], which could be ascribed to the sluggish kinetics of both samples. Due to the removal of impurity by acid washing, the capacity increased from 156 to 200 mAh g^{-1}, with the improved cycling stability as well. After pre-oxidation, ACp showed a capacity of 260 mAh g^{-1}, while the ACp-N-Cl anode exhibited an even higher capacity of 280 mAh g^{-1} and enhanced stability [Supplementary Figure 9A]. A suitable pre-oxidation temperature could better modify the pore structure, introduce oxygen defects, and improve the stability and activity of the carbon structure, thereby affecting the battery performance [Supplementary Figure 9B]. The incorporation of various chloride metal salts all enhanced the battery stability to varying extents [Supplementary Figure 10A], suggesting that chlorine doping was beneficial for improving the stability of the battery. Notably, N species played a dominant role for the enhanced capacity, since its content was much higher than that of Cl. After 50 cycles, the capacity of ACp-N-Cl (220 mAh g^{-1}) significantly surpassed that of ACp (148 mAh g^{-1}), suggesting the introduction of a proper amount of N and Cl species in the carbon dramatically improved its stability [Supplementary Figures 9A, 10B and 11A]. Additionally, the co-doping of N and Br in the carbons also exhibited a similar electrochemical performance, with a capacity of 200 mAh g^{-1} after cycling and comparable to that of ACp-N-Cl [Supplementary Figure 11B], which further confirmed that the incorporation of halogen elements contributed to enhanced material stability. The rate performance graphs of the C, Cp, ACp and ACp-N-Cl electrodes were presented in Figure 4B. The ACp-N-Cl demonstrated average capacities of 265, 214, 198, 182, 164 and 146 mAh g^{-1} at 0.02, 0.05, 0.1, 0.2, 0.5 and 1.0 A g^{-1}, respectively. Upon returning the current to 0.05 A g^{-1}, a high capacity of 228 mAh g^{-1} was retained. Although ACp possessed the highest BET surface area and pore volume, ACp-N-Cl exhibited better electrochemical performances in the aspects of specific capacity, durability, and rate property. This indicated that the improved sodium-storage behavior was not simply determined by a larger specific surface area or pore volume. ACp-N-Cl with the largest average pore size certainly accelerated the transfer of mass and electrolyte, while the heteroatoms and structural defects also played a crucial role during the electrochemical process. The introduction of N and Cl species, along with the decrease of O species, would largely improve the stability of carbon anodes. What's more, these doped N and Cl species also decreased the energy barrier for Na^+ transport superior to O species, as evidenced by the largely decreased electrochemical impedance spectroscopy (EIS) values of ACp-N-Cl than ACp[29]. The EIS spectra were further fitted using an equivalent circuit of R_0-(R_{ct}||CPE)-W_0 [Figure 4C], where R_0 is the ohmic resistance, R_{ct} is the charge-transfer resistance mainly contributed by the electrochemical reaction at the electrode/electrolyte interface, CPE is the constant phase element, and W_0 is the Warburg impedance. The EIS curves before and after fitting are presented in Supplementary Figures 12 and 13, and the corresponding detailed parameters are provided in Supplementary Table 7. The fitted R_{ct} value of ACp-N-Cl was 898.4 Ω, which was much lower than those of C (4,006 Ω), Cp (2,991 Ω), and ACp (2,241 Ω), indicating faster interfacial charge transfer and improved electrochemical kinetics. This advantage was accompanied by the smallest R_0 value for ACp-N-Cl. Figure 4D presented the CV curves between 0.01-3.0 V under a sweep speed of 0.2 mV s^{-1}. With the continuous modification of the samples from the C to ACp-N-Cl, the capacitance gradually increased, which was consistent with the trend of capacity change. Nearly no reduction peaks were observed for C and Cp in CV profiles. In contrast, both ACp and ACp-N-Cl exhibited broad reduction peaks located at ~0.6 V, which may be caused by the incorporation of oxygen-containing functional groups that provided additional sodium storage sites during the electrochemical reaction processes, thus improving the sodium storage capability[30,31]. Figure 4E presented the capacities of different samples at 1 A g^{-1}. The initial capacities of C and Cp were extremely low, indicating their inferior electrochemical performance under high-current-density conditions. By contrast, ACp and ACp-N-Cl exhibited initial capacities of 112 and 126 mAh g^{-1}, respectively. The incorporation of heteroatoms such as O, N or Cl is generally regarded as a defect-engineering strategy, thereby enhancing the rate capability at high current densities and improving the overall battery capacity[32,33]. However, compared to O-related defects, the N and Cl species were more active for Na^+ storage, since the high-rate performance and long-term stability of ACp-N-Cl were greatly improved

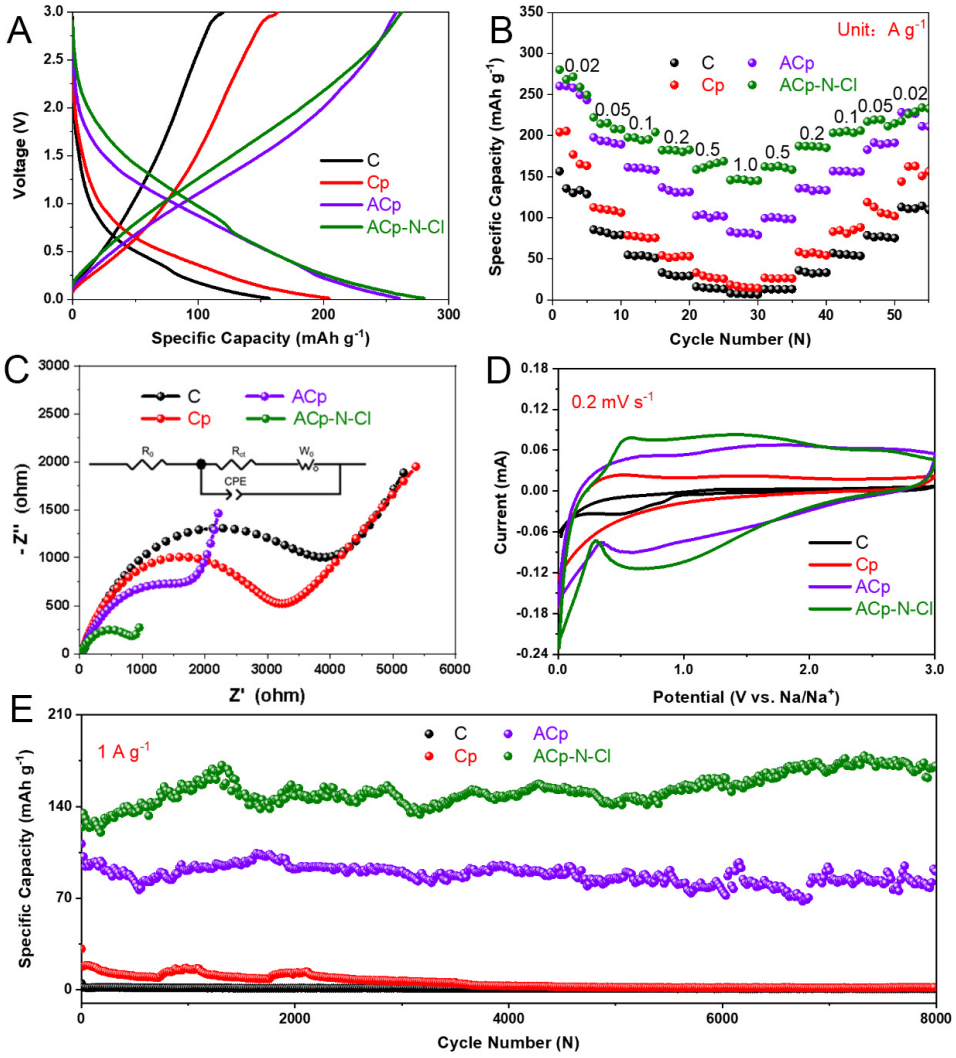

Figure 4. (A) Charge-discharge curves, (B) multiplication rate performance, (C) EIS spectra, (D) CV curves and (E) stability test at 1 A g^{-1} of C, Cp, ACp and ACp-N-Cl. EIS: Electrochemical impedance spectroscopy; CV: cyclic voltammetry.

when part of O atoms were replaced by N and Cl species. Thus, the ACp-N-Cl maintained a satisfactory capacity of 173 mAh g^{-1} even cycled for 8,000 cycles, which was much higher than that of ACp (97 mAh g^{-1}).

To further analyze the Na-storage behavior of the anodes, CV curves of C and ACp-N-Cl were tested at various scan rates from 0.4 to 1.2 mV s^{-1} [Figure 5A and Supplementary Figure 14A].

The relationship between peak current and scan rate followed the equations below[34]:

$$i = av^b \quad (1)$$

$$\log(i) = b\log(v) + \log(a) \quad (2)$$

where i is the peak current (mA), v represents the scan rate (mV s^{-1}), and a and b are adjustable parameters. The value of b represents the slope of the linear plot of log(i) versus log(v). When b is close to 0.5, the process is diffusion-controlled, whereas a surface capacitive behavior was dominated when b approaches 1.0[35]. The b values of the cathodic and anodic peaks [Figure 5B and Supplementary Figure 14B] for C and ACp-N-Cl

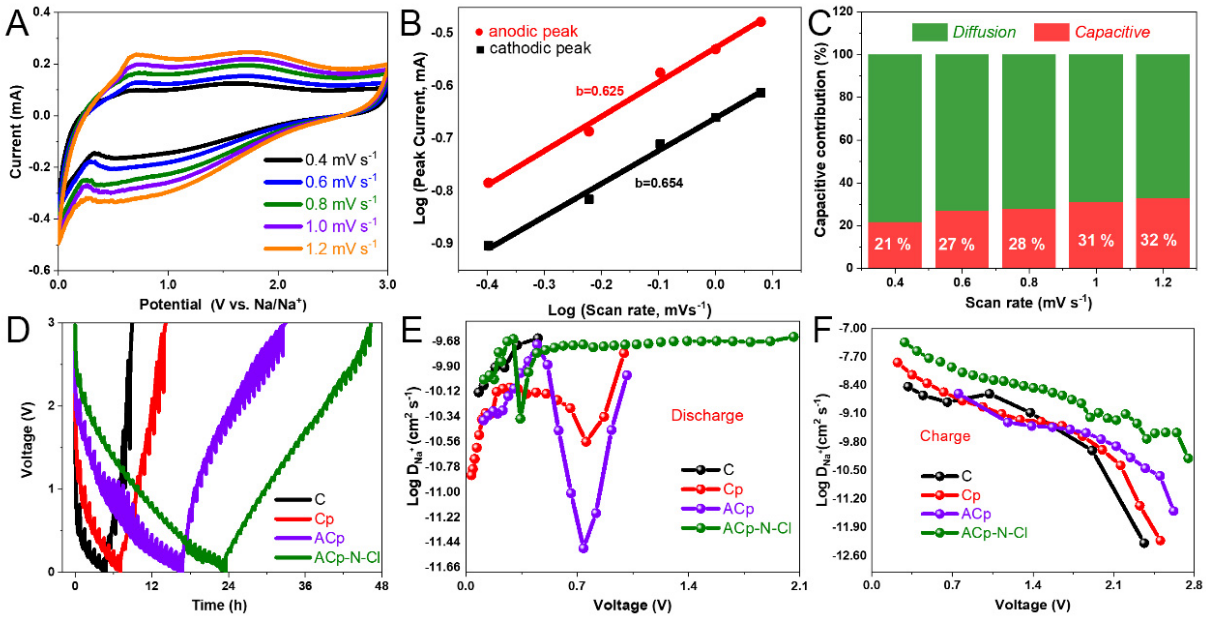

Figure 5. (A) CV curves, (B) the corresponding b values for cathodic and anodic peaks, and (C) percentage of surface capacitance contribution at different sweep rates of ACp-N-Cl, (D) GITT curves, and the calculated D_{Na+} during (E) discharge and (F) charge processes of the samples. CV: Cyclic voltammetry; GITT: galvanostatic intermittent titration technique.

were 0.703, 0.654, 0.590 and 0.625, respectively, suggesting that their electrochemical processes were under mixed control, primarily governed by diffusion with partial capacitive contribution. Although the capacitive contribution ratio of the C and ACp-N-Cl continuously increased with increasing scan rate [Figure 5C and Supplementary Figures 14C, 15 and 16], diffusion control still remained the dominant, consistent with the b-value analysis. Unexpectedly, with scan rates of 0.4, 0.6, 0.8, 1.0, and 1.2 mV s^{-1}, the pseudocapacitive contributions of the C were 3.8%, 5.2%, 5.3%, 5.4%, and 6.0%, respectively. This suggested that the process was nearly entirely governed by diffusion, which consequently resulted in extremely sluggish kinetics. After treatment with NH_4Cl, the pseudocapacitive contributions significantly increased, ranging from 21% to 32% with the increase of scan rates from 0.4 to 1.2 mV s^{-1}. Generally, a diffusion-controlled process is typically unfavorable for the high-rate discharge capability, the observed enhancement in rate performance suggested that the defects generated by N and Cl doping and the pore size enlarged by etching would facilitate the sodium storage and increase its capacitive contribution, which in turn improved the high-current discharge capability[36]. The GITT, which comprised a sequence of galvanostatic pulse and relaxation processes, was employed to determine the apparent chemical diffusion coefficient of Na^+ (D_{Na^+}) within the electrodes. The test was performed at 0.02 A g^{-1} with a pulse duration of 30 min and a relaxation interval of 15 min. The value of D_{Na^+} in different samples was calculated based on Fick's second law with the simplified equation[37]:

$$D = \frac{4}{\pi\tau}\left(\frac{m_B V_M}{M_B S}\right)^2\left(\frac{\Delta E_S}{\Delta E_\tau}\right)^2 \quad (3)$$

where τ denotes the pulse duration, M_B represents the mass of active material, V_M is the molar volume of carbon, M_B corresponds to the molar mass of carbon, and S refers to the electrode surface area. ΔE_S and ΔE_τ can be obtained from the GITT profiles. GITT and the D_{Na+} values derived from the discharge and charge processes are shown in Figure 5D and E. Compared with C, Cp, and ACp, ACp-N-Cl showed smaller pulse-voltage changes and faster relaxation toward equilibrium at each step, indicating lower ohmic/interfacial

polarization and smaller transport resistance. The resulting log D_{Na+} values [Figure 5E and F] showed that ACp-N-Cl generally exhibited higher diffusion coefficients over most potential regions during charge and discharge, suggesting faster Na^+ diffusion kinetics, which was beneficial for operation at high current densities[38].

To investigate the changes in the battery after cycling, the electrodes after 50 cycles at 0.02 A g^{-1} were characterized by SEM and XRD, and the post-cycling CV and EIS were also measured. Cracks and fissures appeared on the electrode surface compared with the pristine electrode [Figure 6A and Supplementary Figure 17], along with the formation of numerous flake-like and needle-like substances that were distinguished from the glass fiber separator with a micro-sized fiber morphology [Figure 6B and Supplementary Figure 18]. This phenomenon could be ascribed to sodium species intercalated within the carbon matrix, which were not completely extracted after discharge[39]. As evidenced by EDS mapping results, abundant Na elements were detected in addition to the previously observed C, N, O, and Cl elements. To have further insights into used electrode materials, the XRD pattern of the electrode after cycling was shown in Figure 6C. The results revealed that, apart from the peaks corresponding to aluminum (Al), only an obvious carbon peak at 26.5° was observed, with no other diffraction peaks detected, suggesting the existence of trace amounts of sodium species on the surface. Compared with the carbon peak at 24.93° [Supplementary Table 3] before cycling, the peak shifted to a higher angle after cycling, which may be attributed to electrochemical stress-induced rearrangement of disordered carbon structures into a more ordered configuration[40]. The CV curve after cycling [Figure 6D] showed a decrease in capacitive area and the disappearance of distinct redox peaks, which was consistent with the capacity decrease observed in the charge-discharge curves at 0.02 A g^{-1}. This evolution also suggested that the material stabilized upon cycling, which could also be related to defect passivation or the partial loss of electrochemically active sites during cycling. Unexpectedly, the R_{ct} value of the battery decreased by half after cycling, from 898.4 Ω to 364.9 Ω [Figure 6E, Supplementary Figures 19 and 20 and Supplementary Tables 7 and 8], which might be attributed to the improved electrolyte infiltration and the stabilization of ACp-N-Cl during charge and discharge processes[41]. Meanwhile, the R_0 resistance also decreased from 19.67 Ω to 17.80 Ω, indicating a reduction in the internal contact resistance of the battery. Those changes also likely explained the gradual capacity increase observed during cycling test at 1 A g^{-1}.

CONCLUSIONS

The simple calcination of anthracite with NH_4Cl at 400 °C resulted in the formation of a high-performance carbon engineered with N and Cl heteroatoms, which largely improved its specific capacity and durability. Driven by the doped N and Cl species, the rate performance of this kind of carbon anode for Na^+ storage was greatly enhanced. As a result, the obtained ACp-N-Cl with the largest number of defect sites exhibited excellent stability and delivered a high specific capacity of 220 mAh g^{-1} (@0.02 A g^{-1}) after 50 cycles. Additionally, the ACp-N-Cl exhibited a discharge capacity of 173 mAh g^{-1} (@1 A g^{-1}) even after 8,000 cycles, superior to most reported hard carbons and their functional products. This study provides a green and facile approach for designing high-performance, low-cost SIB anode materials and may promote the practical application of SIBs in energy storage systems.

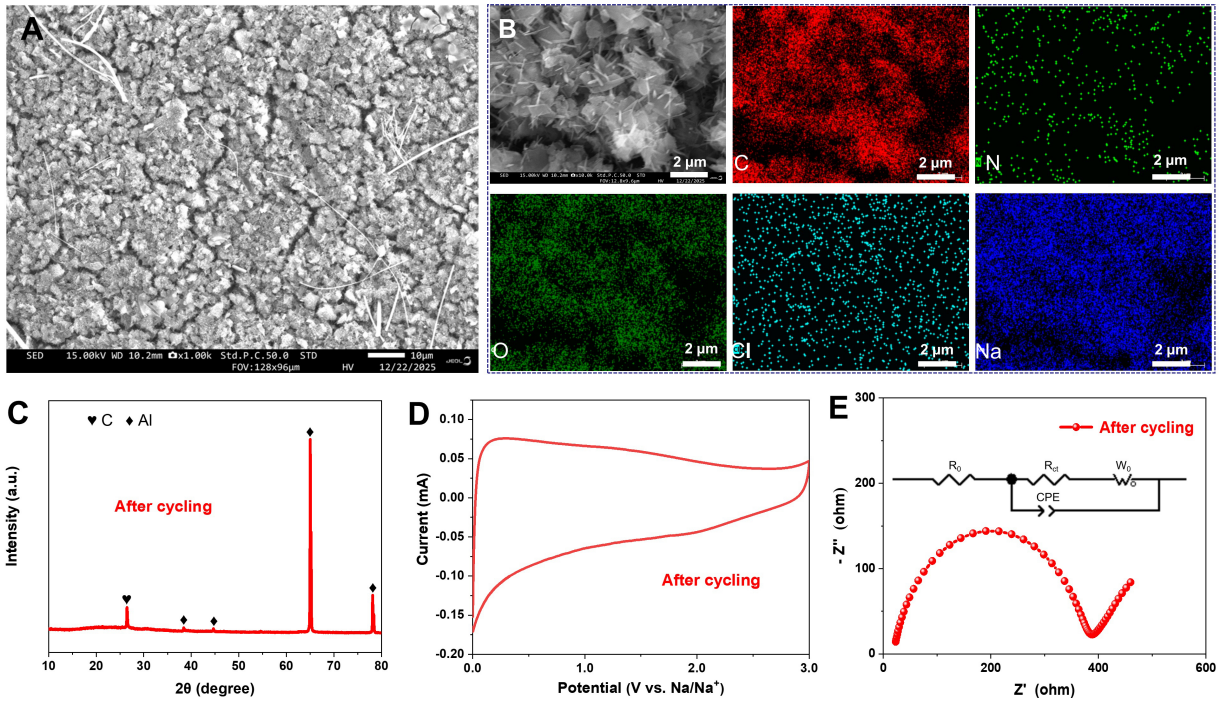

Figure 6. (A) SEM; (B) EDS mapping images; (C) XRD; (D) CV curve and (E) EIS spectrum of ACp-N-Cl after cycling upon discharging to 0.01 V. SEM: Scanning electron microscopy; EDS: XRD: X-ray diffraction; CV: cyclic voltammetry; EIS: electrochemical impedance spectroscopy.

DECLARATIONS

Author's contributions

Writing-original draft: Zou, L.; Yang, T.; Li, L.
Investigation: Zou, L.; Yang, T.; Li, L.; Lin, L.; Jing, M.
Formal analysis: Zou, L.; Yang, T.; Li, L.; Lin, L.; Jing, M.
Funding acquisition: Zou, L.; Lin, L.; Jing, M.; Wang, Q.
Discussion: Zou, L.; Yang, T.; Wang, Q.
Writing-review & editing: Wang, Q.

Availability of data and materials

The data that support the findings of this study are available from the corresponding authors upon reasonable request.

AI and AI-assisted tools statement

Not applicable.

Financial support and sponsorship

The work described in this paper was financially supported by the National Natural Science Foundation of China (No. 22409073) and Jiangsu University (4023000085).

Conflicts of interest

The authors declared that there are no conflicts of interest.

Ethical approval and consent to participate

Not applicable.

Consent for publication

Not applicable.

Copyright

Supplementary Materials

Supplementary Materials

REFERENCES

1. Lou, Z.; Wang, H.; Wu, D.; et al. Microcrystalline regulation of bituminous coal derived hard carbon by pre-oxidation strategy for improved sodium-ion storage. *Fuel* **2022**, *310*, 122072. DOI
2. Xiao, J.; Li, X.; Tang, K.; et al. Recent progress of emerging cathode materials for sodium ion batteries. *Mater. Chem. Front.* **2021**, *5*, 3735-64. DOI
3. Chen, Y.; Kang, Y.; Zhao, Y.; et al. A review of lithium-ion battery safety concerns: the issues, strategies, and testing standards. *J. Energy. Chem.* **2021**, *59*, 83-99. DOI
4. Liu, Y.; He, Q.; Shi, X.; Zhang, Q.; An, X. Energy storage in China: development progress and business model. *J. Energy. Storage.* **2023**, *72*, 108240. DOI
5. Fan, X.; Kong, X.; Zhang, P.; Wang, J. Research progress on hard carbon materials in advanced sodium-ion batteries. *Energy. Storage. Mater.* **2024**, *69*, 103386. DOI
6. Li, R.; Su, C.; Yang, W.; et al. Molecular level modulation of anthracite-based hard carbon precursors for efficient sodium-ion batteries. *Chem. Eng. J.* **2025**, *506*, 159968. DOI
7. Liu, K.; Ji, S.; Liu, B.; et al. Recent advances on coal-based hard carbon anode materials for sodium-ion batteries. *Nano. Res.* **2025**, *18*, 94907625. DOI
8. Zhang, Y.; Xiong, D.; Xie, Y.; Wang, Q.; Feng, Z. Regulating the microcrystalline structure of anthracite via thermal treatment strategies for enhanced sodium-ion storage performance. *Ionics* **2025**, *32*, 1923-33. DOI
9. Wang, B.; Xia, J.; Dong, X.; Wu, X.; Jin, L.; Li, W. Highly purified carbon derived from deashed anthracite for sodium-ion storage with enhanced capacity and rate performance. *Energy. Fuels.* **2020**, *34*, 16831-7. DOI
10. Sun, C.; Zhang, X.; An, Y.; et al. Low-temperature carbonized nitrogen-doped hard carbon nanofiber toward high-performance sodium-ion capacitors. *Energy. Environ. Mater.* **2023**, *6*, e12603. DOI
11. Wu, C.; Yang, Y.; Zhang, Y.; et al. Hard carbon for sodium-ion batteries: progress, strategies and future perspective. *Chem. Sci.* **2024**, *15*, 6244-68. DOI PubMed PMC
12. Zhao, X.; Liu, P.; Xu, J.; Sheng, S.; Jia, L.; Chen, Z. *In-situ* catalytic dehydration construction of hierarchical nano microporous carbon with NH_4Cl for supercapacitors and zinc ion hybrid capacitors. *J. Power. Sources.* **2025**, *632*, 236238. DOI
13. Wang, Y.; Li, H.; Yang, W.; Jian, S.; Zhang, C.; Duan, G. One step activation by ammonium chloride toward N-doped porous carbon from camellia oleifera for supercapacitor with high specific capacitance and rate capability. *Diamond. Relat. Mater.* **2022**, *130*, 109526. DOI
14. Chen, Z.; Wang, X.; Li, W.; Yang, X.; Qiu, J.; Wang, Z. A low-temperature dehydration carbon-fixation strategy for lignocellulose-based hierarchical porous carbon for supercapacitors. *ChemSusChem* **2021**, *15*, e202101918. DOI
15. Zhou, Y.; Zhou, P.; Tang, X.; et al. Mesoporous carbon-encapsulated Co single atoms synthesized via NH_4 Cl-templated ZnCo-ZIF pyrolysis for efficient ammonium perchlorate catalysis. *Inorg. Chem. Front.* **2026**, *13*, 690-700. DOI
16. Qiu, T.; Xie, W.; Bai, X.; Li, C.; Zhang, N. Study on the formation mechanism of a core-shell structure during graphitization of anthracite. *ACS. Omega.* **2024**, *9*, 22581-9. DOI
17. Xu, Y.; Guo, D.; Luo, Y.; et al. Constructing abundant oxygen-containing functional groups in hard carbon derived from anthracite for high-performance sodium-ion batteries. *Nanomaterials* **2023**, *13*, 3002. DOI PubMed PMC
18. Kim, J.; Han, S.; Koo, B.; Lee, S.; Yang, J. Structure dependent electrochemical behaviors of hard carbon anode materials derived from natural polymer for next-generation sodium ion battery. *Polymers* **2023**, *15*, 4373. DOI PubMed PMC
19. Zhang, G.; Zhang, L.; Ren, Q.; et al. Tailoring a phenolic resin precursor by facile pre-oxidation tactics to realize a high-initial-coulombic-efficiency hard carbon anode for sodium-ion batteries. *ACS. Appl. Mater. Interfaces.* **2021**, *13*, 31650-9. DOI
20. Yi, S.; Yuan, M.; Li, B.; Hu, X.; Zhang, H.; Hou, Z. Optimization of acid modifier and its effect on the wettability of anthracite coal. *Sci. Rep.* **2025**, *15*, 14189. DOI PubMed PMC
21. Wang, Y.; Li, M.; Zhang, Y.; Zhang, N. Hard carbon for sodium storage: Mechanism and performance optimization. *Nano. Res.* **2024**, *17*, 6038-57. DOI
22. Yu, K.; Wang, X.; Yang, H.; Bai, Y.; Wu, C. Insight to defects regulation on sugarcane waste-derived hard carbon anode for sodium-ion batteries. *J. Energy. Chem.* **2021**, *55*, 499-508. DOI

23. Gengenbach, T. R.; Major, G. H.; Linford, M. R.; Easton, C. D. Practical guides for X-ray photoelectron spectroscopy (XPS): interpreting the carbon 1s spectrum. *J. Vac. Sci. Technol. A:. Vac. Surf. Films.* **2021**, *39*, 013204. DOI
24. Jiang, J.; Shen, Q.; Chen, Z.; Wang, S. Nitrogen-doped porous carbon derived from coal for high-performance dual-carbon lithium-ion capacitors. *Nanomaterials* **2023**, *13*, 2525. DOI PubMed PMC
25. Deng, J.; Peng, Z.; Xiao, Z.; Song, S.; Dai, H.; Li, L. Porous doped carbons from anthracite for high-performance supercapacitors. *Appl. Sci.* **2020**, *10*, 1081. DOI
26. Li, J.; Chen, Y.; He, S.; Yang, Y.; Wang, Y.; Guo, L. High performance $Na_3V_2(PO_4)_3$ with nitrogen-chlorine co-doped carbon matrix *in-situ* synthesized in chitosan quaternary ammonium hydrogel for sodium ion batteries. *Chem. Eng. J.* **2023**, *452*, 139311. DOI
27. Xiang, X.; Lin, Y.; Li, B.; Sun, S.; Zhu, X. High-performance porous carbon electrode materials derived from air pre-oxidation of anthracite supplemented with KOH activation for supercapacitors. *J. Electron. Mater.* **2023**, *52*, 6172-81. DOI
28. Takehira, H.; Karim, M. R.; Shudo, Y.; Fukuda, M.; Mashimo, T.; Hayami, S. Modulating the work function of graphene by pulsed plasma aided controlled chlorination. *Sci. Rep.* **2018**, *8*, 17392. DOI PubMed PMC
29. Li, Y.; Yang, Y.; Lin, R.; et al. Enhancing electrochemical performance in sodium-ion batteries: Strategic modification of oxygen-containing functional groups in hard carbon. *Fuel* **2025**, *381*, 133397. DOI
30. Zhou, Z.; Wang, Z.; Fan, L. *In-situ* capture defects through molecule grafting assisted in coal-based hard carbon anode for sodium-ion batteries. *Chem. Eng. J.* **2024**, *490*, 151428. DOI
31. Wang, Y.; Li, M.; Zhang, Y.; Zhang, N. Defect-rich hard carbon designed by heteroatom escape assists sodium storage performance for sodium-ion batteries. *Chem. Eng. J.* **2024**, *499*, 156115. DOI
32. Xu, T.; Qiu, X.; Zhang, X.; Xia, Y. Regulation of surface oxygen functional groups and pore structure of bamboo-derived hard carbon for enhanced sodium storage performance. *Chem. Eng. J.* **2023**, *452*, 139514. DOI
33. Fan, L.; Zhang, X.; Fan, L.; et al. Boosting the high capacitance-controlled capacity of hard carbon by using surface oxygen functional groups for fast and stable sodium storage. *ACS. Appl. Energy. Mater.* **2021**, *4*, 11436-46. DOI
34. Jiang, Z.; Xing, B.; Qu, X.; et al. Anthracite-based expanded graphite as anode materials for sodium-ion batteries with exceptional sodium storage performances. *J.. Energy. Storage.* **2024**, *83*, 110667. DOI
35. Eren, E. O.; Senokos, E.; Song, Z.; et al. Hard carbon from a sugar derivative for next-generation sodium-ion batteries. *Mater. Horiz.* **2025**, *12*, 886-98. DOI PubMed PMC
36. Liu, X.; Li, J.; Liu, Z.; Nong, G. N/Cl co-doped porous carbon materials based on choline chloride for supercapacitors. *J. Alloys. Compd.* **2025**, *1032*, 181264. DOI
37. Li, B.; Liu, J.; Xiu, X.; Yang, G.; Zhu, K. Insights into the charge storage mechanism of $Na_3V_2(PO_4)_3$ cathode in sodium-ion batteries. *Bull. Mater. Sci.* **2023**, *46*, 97. DOI
38. Hou, S.; Zhang, D.; Lei, Y.; et al. Regulating closed pore structure of coal-based hard carbon anode by preoxidation for high-rate performance sodium-ion batteries. *Langmuir* **2025**, *41*, 4259-69. DOI
39. Liu, Y.; Yin, J.; Wu, R.; et al. Molecular engineering of pore structure/interfacial functional groups toward hard carbon anode in sodium-ion batteries. *Energy. Storage. Mater.* **2025**, *75*, 104008. DOI
40. Sun, L.; Li, J.; Liu, D.; Wang, L. Precision structural modulation and sodium cluster operando presodiation for high-performance hard carbon anode with fast kinetics in sodium-ion batteries. *Chem. Eng. J.* **2025**, *525*, 170591. DOI
41. Li, P.; Li, X.; Yang, X.; et al. Oxygen activation-induced mesoporous structure: enhancing the rate performance of hard carbon anode materials in sodium-ion batteries. *Ionics* **2025**, *31*, 4333-41. DOI